A source of polarization-entangled photon pairs interfacing quantum memories with telecom photons

C Clausen[1,3], F Bussières[1], A Tiranov[1], H Herrmann[2], C Silberhorn[2], W Sohler[2], M Afzelius[1] and N Gisin[1]

[1] Group of Applied Physics, University of Geneva, CH-1211 Geneva 4, Switzerland
[2] Applied Physics / Integrated Optics Group, University of Paderborn, D-33095 Paderborn, Germany
E-mail: christoph.clausen@ati.ac.at and felix.bussieres@unige.ch

Abstract

We present a source of polarization-entangled photon pairs suitable for the implementation of long-distance quantum communication protocols using quantum memories. Photon pairs with wavelengths 883 nm and 1338 nm are produced by coherently pumping two periodically poled nonlinear waveguides embedded in the arms of a polarization interferometer. Subsequent spectral filtering reduces the bandwidth of the photons to 240 MHz. The bandwidth is well-matched to a quantum memory based on an Nd:YSO crystal, to which, in addition, the center frequency of the 883 nm photons is actively stabilized. A theoretical model that includes the effect of the filtering is presented and accurately fits the measured correlation functions of the generated photons. The model can also be used as a way to properly assess the properties of the source. The quality of the entanglement is revealed by a visibility of $V = 96.1(9)\%$ in a Bell-type experiment and through the violation of a Bell inequality.

Keywords: parametric downconversion, entanglement, quantum communication, quantum memory, nonlinear waveguide

[3] Present address: Vienna Center for Quantum Science and Technology, TU Wien-Atominstitut, Stadionallee 2, A-1020 Vienna, Austria.

1. Introduction

Spontaneous parametric down-conversion (SPDC) is a simple and efficient technique for the generation of non-classical light and of photonic entanglement. Several important tasks of quantum communication require photonic entanglement, but also optical quantum memories to store this entanglement [1]. A prominent example is the quantum repeater [2, 3], which can extend the transmission distance of entanglement beyond the hard limit dictated by loss in optical fibre. In this context, the combination of photon pair sources and multimode quantum memories was proposed [4]. The essence of this proposal is that the sources create pairs comprised of one telecom-wavelength photon that is used to distribute entanglement between distant nodes, while the other photon is stored in a nearby quantum memory. This increases the probability of successfully heralding a stored photon when the telecom photon is detected. Multimode storage with selective recall then multiplies the entanglement distribution rate by the number of stored modes, and is essential to reach practical rates over distances of 500 km or more [3].

Creating photon pairs such that one photon exactly matches the absorption profile of the quantum memory, while the other is within a telecom wavelength window of standard optical fibre, is a challenging task in itself. Sources of photon pairs based on emissive atomic ensembles or single emitters [3] typically generate photons at wavelengths in the vicinity of 800 nm, where the loss in standard optical fibre is on the order $\sim$3 dB km^{-1}, i.e. at least ten times larger than in telecom fibres. Reaching telecom wavelengths with such sources therefore requires frequency conversion techniques, which has been demonstrated [5–10], but imposes an important technical overhead. SPDC offers much more flexibility, since the wavelengths of the pump can be easily chosen (and tuned) to directly generate the desired wavelengths. However, unfiltered SPDC photons have a bandwidth on the order of hundreds of GHz or more. Hence, they still need to be spectrally filtered to the memory absorption bandwidth, which typically ranges from a few MHz to a few GHz at most [1].

Different approaches for the filtering of SPDC photons were demonstrated. Direct filtering (using Fabry–Perot cavities) of frequency-degenerate photon pairs created in a lithium niobate waveguide was first demonstrated [11], and used for storage of an heralded photon on the D_1 line (795 nm) of cold rubidium atoms. The high conversion efficiency of the waveguide was here used to counterbalance the extreme filtering (down to 9 MHz), which effectively rejects almost all of the generated SPDC bandwidth. A similar source was also developed to demonstrate the heralded single-photon absorption by a single calcium atom at 854 nm [12]. Another approach is based on pumping a bulk crystal put inside a cavity, yielding a doubly resonant optical parametric oscillator (OPO) operated far below threshold. The cavity effectively enhances the length of the nonlinear medium, and is well-suited to generate narrowband photons. This was first demonstrated with frequency-degenerate photons resonant with the D_2 line of rubidium (780 nm) [13, 14], and later with photons resonant with the D_1 line (795 nm) [15]. It was also demonstrated with photon pairs generated at 1436 nm and 606 nm [16], and used for storage in a praseodymium-doped crystal [17]. One important technical difficulty in using an OPO is to fulfil the doubly resonant condition and simultaneously lock one photon's frequency on the quantum memory. Even though such sources can in principle emit the photons in a single longitudinal mode with the help of the clustering effect [18, 19], current state-of-the-art sources [16, 20, 21] do not yet achieve all the requirements, and in

practice some additional filtering outside of the cavity is still necessary to remove spurious longitudinal modes.

All the aforementioned experiments produced photons with linewidths $\Delta\nu$ ranging from 1 to 20 MHz, which is dictated by the absorption bandwidth of the respective quantum memory they were developed for. The coherence time $\tau_c \sim 1/\Delta\nu$ of the photons produced can therefore be as long as a microsecond, which impacts on the rate at which those photons can be distributed. It is therefore desirable for the quantum memory to absorb over a large bandwidth to increase the photon distribution rate.

In this article, we present a CW-pumped source of polarization-entangled photon pairs with 240 MHz linewidth using a direct filtering approach. This source was designed for experiments involving quantum memories based on the atomic frequency comb (AFC) protocol [22] in a Nd:YSO crystal. Earlier versions of this source produced energy-time entangled photons with a smaller linewidth, and was used to demonstrate the quantum storage of photonic entanglement in a crystal [23], heralded entanglement of two crystals [24] and the storage of heralded polarization qubits [25]. Recently, the source described in this paper was used to demonstrate the teleportation from a telecom-wavelength photon to a solid-state quantum memory [26]. We note that a similar source, based on a pulsed pump, was used for the storage of broadband time-bin entangled photons in a Tm : LiNbO$_3$ waveguide [27].

The paper is organized as follows. We give the requirements for the photon-pair source in section 2. The concept behind the implementation is given in section 3 with the details of the actual implementation following in section 4. In section 5 the spectral properties and the correlation functions of the filtered photons are presented and compared to the predictions of a model that includes the effect of the filtering. The efficiency and detection rate of the source is presented in section 6. Section 7 presents measurements showing the high degree of polarization entanglement of the photon pairs, as well as its nonlocal nature. The appendices contain all the details pertaining to the characterization of the source.

2. Requirements

The source was designed for experiments involving an AFC type of quantum memory in a Nd:YSO crystal, so the *signal* photon of a pair has to be in resonance with the transition from the $^4I_{9/2}$ ground state to the $^4F_{3/2}$ excited state of the Nd^{3+} ion at $\lambda_s = 883$ nm. Quantum communication over long distances in optical fibre requires the wavelength of the idler photon of a pair to be inside one of the so-called telecom windows, which span the region from 1300 nm to 1700 nm. The condition for the idler wavelength can be conveniently satisfied using a pump wavelength of $\lambda_p = 532$ nm, for which high-quality solid-state lasers are readily available. This places the idler wavelength at $\lambda_i = (\lambda_p^{-1} - \lambda_s^{-1})^{-1} = 1338$ nm.

The bandwidth of the generated photon pairs is dictated by the bandwidth of the quantum memory. In earlier experiments this bandwidth was 120 MHz [23, 24]. Recently it has been increased to about 600 MHz [26]. Although this is fairly large for a quantum memory, it is still three orders of magnitude narrower than the typical bandwidth of photons generated by SPDC, which is given by the phasematching condition and can be as large as 1 THz.

We also require quantum entanglement between the signal and idler photons. Entanglement can be established between various degrees of freedom. In particular energy-time entanglement is intrinsically present when using a highly coherent pump laser. In this
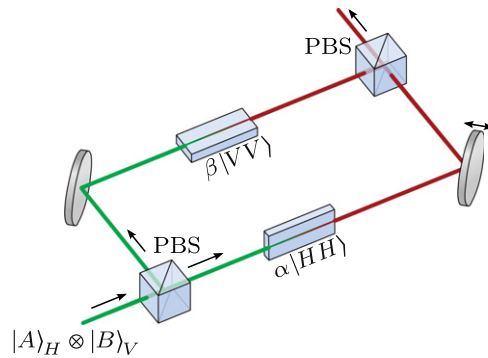
Figure 1. Creation of polarization-entangled photon pairs with the help of two waveguides inside a polarization interferometer. A PBS coherently splits the pump photons according to their polarization. Each polarization component has a certain probability to be converted into a photon pair with the same polarization. The two polarization components of the photon pair are then recombined into the same spatial mode by a second PBS. The relative phase can be adjusted by moving one of the mirrors.

work, however, we focus on polarization entanglement because of the experimental convenience in manipulating and measuring the polarization state of light.

3. Concept

Various schemes have been devised to generate polarization-entangled photon pairs through SPDC. These schemes include selective collection of photon pairs emitted at specific angles for non-collinear type-II phasematching [28], collinear SPDC in two orthogonally oriented crystals [29, 30], and SPDC in Sagnac interferometers [31, 32]. We wanted to extend our existing and well-functioning waveguide source [23], which is inherently collinear, to a configuration that can create polarization-entangled photon pairs. Putting two waveguides back to back is in principle possible, but as the cross-section of the waveguides is only a few micrometres and may vary from waveguide to waveguide, efficient and stable coupling from one to the other is experimentally extremely challenging. Using a waveguide in a Sagnac configuration is complicated by the need for achromatic optics for coupling into and out of the waveguide and for the necessary polarization rotation.

   To be able to efficiently employ our waveguides we follow the ideas of [33, 34] that suggest using a nonlinear crystal in each arm of a polarization interferometer, as sketched in figure 1. We consider the situation of type-I phasematching and that the two nonlinear crystals may have different down-conversion efficiencies. Let the photons from the pump laser be in a polarization state $|A\rangle_H \otimes |B\rangle_V$, where $|A\rangle_H$ corresponds to a horizontally polarized coherent state of complex amplitude A, and similarly for $|B\rangle_V$. A polarizing beam splitter (PBS) at the entrance of the interferometer splits the two coherent state components in two paths. In the horizontal path the photons can be converted into a photon pair $|HH\rangle$ with a probability amplitude $\alpha \propto A$ by a first nonlinear waveguide. A second waveguide rotated by 90° in the vertical path can produce a photon pair $|VV\rangle$ with probability amplitude $\beta \propto B$. Another PBS recombines the two paths, and the final single-pair state $|\psi_1\rangle$ is given by

Table 1. A selection of the parameters of the two waveguides for direct comparison.

	Waveguide	
	PPKTP	PPLN
Supplier	AdvR Inc.	University of Paderborn
Poling period	$8.2\,\mu$m	$6.45\,\mu$m
Length of poled region	13 mm	50 mm
Waveguide width	$\sim 4\,\mu$m	$\sim 6\,\mu$m
Waveguide height	$\sim 7\,\mu$m	$\sim 6\,\mu$m
Phase-matching temperature	$\sim 53\,°$C	$\sim 173\,°$C

$$|\psi_1\rangle \propto |\alpha||HH\rangle + \mathrm{e}^{\mathrm{i}\phi}\,|\beta||VV\rangle, \tag{1}$$

where the phase ϕ depends on the path-length difference of the interferometer, and on the relative phase between α and β. By choosing the pump polarization such that it compensates the efficiency difference, i.e. $|\alpha| = |\beta|$, and by slightly varying the position of one of the mirrors to obtain $\mathrm{e}^{\mathrm{i}\phi} = \pm 1$, the single-pair state becomes equivalent to one of the two Bell-states $|\Phi_\pm\rangle = (|HH\rangle \pm |VV\rangle)/\sqrt{2}$. However, one could equally well produce non-maximally entangled states by choosing the polarization of the pump laser accordingly.

4. Implementation

In the following we detail the actual implementation of the source of polarization-entangled photon pairs. We start by describing the two waveguides that have been used. We then discuss the problem of matching the spatial modes of the photons with the same wavelength from different waveguides. Next, we consider the relative phase ϕ in equation (1). Finally, we describe the measures taken to reduce the bandwidth of the photons.

4.1. The waveguides

Waveguides are used instead of bulk crystals because they yield a much higher conversion efficiency. This is necessary because the spectral filtering we apply is much narrower than the intrinsic spectral width of the down-conversion process, so only a small fraction of the pump power is used to create photons in the desired spectral range. Hence, the larger conversion efficiency essentially compensates the loss in power of the pump.

The photon pair source is based on two nonlinear waveguides made from different materials and with different parameters. The choice of using two different types of waveguides was made for practical reasons that are not important for the results presented in this paper. However, this choice allows for a direct comparison of the performance of the two waveguides. A selection of parameters for the two waveguides is shown in table 1.

The first waveguide was obtained from AdvR Inc. and has been fabricated in a chip of periodically poled potassium titanyl phosphate (PPKTP) by ion exchange. The chip contains a collection of identical waveguides of width and height approximately $4\,\mu$m and $7\,\mu$m, respectively. Each waveguide spans the entire 13 mm length of the chip. The poling period of $8.2\,\mu$m allows to achieve type-I phase matching for the signal and idler wavelengths of 883 nm and 1338 nm at a temperature of about $53\,°$C. The chip is heated to this temperature using a

custom oven based on a thermo-electric cooler. No dielectric coatings have been applied to the end faces of the chip. We previously used this waveguide, henceforth referred to as the PPKTP waveguide, for the generation of narrowband photon pairs in a series of experiments with solid-state quantum memories [23–25].

The second waveguide was custom designed at the University of Paderborn. It was fabricated by titanium indiffusion on a periodically poled lithium niobate (PPLN) chip. The chip is 62 mm long and contains 25 groups of 50 mm long regions with poling periods between 6.40 μm–6.75 μm. Within each group there are three waveguides of 5 μm, 6 μm and 7 μm width, respectively. We achieved the best results with a waveguide of poling period 6.45 μm and 6 μm width, where the temperature for type-I phase matching at the desired wavelengths is about 173 °C. The chip is heated to this temperature with the help of an oven by Covesion Ltd, which has been slightly modified to accommodate the long chip. The elevated temperature is chosen to mitigate the deterioation of the phasematching by photorefraction.

The custom design of the second waveguide, from now on called the PPLN waveguide, allowed for the addition of a number of features which make it especially suitable for SPDC at the desired wavelengths. On the input side, a $\lambda/4$ SiO$_2$-layer has been applied to the input face to provide an anti-reflective coating for the pump laser at 532 nm. Additionally, the input side has a 12 mm long region without periodic poling where the waveguide width is linearly increased from 2 μm to the final width. Such a taper should facilitate the coupling of the pump laser to the fundamental spatial mode of the waveguide. The output side of the chip has been coated with a 15-layer SiO$_2$/TiO$_2$ stack optimized for high reflection of the pump light and high transmission of the signal and idler photons. Measurements on a reference mirror that was coated simultaneously with the chip revealed reflectivities of 94%, 2.4% and 12% at 532 nm, 880 nm and 1345 nm, respectively.

4.2. Matching of the spatial modes

To obtain a high degree of entanglement between the photon pairs generated in the two waveguides, it is essential that the spatial mode of the photon does not reveal in which waveguide it has been created. A small mismatch can be corrected with a suitable spatial-mode filter, such as a single-mode optical fiber. If, however, the mismatch is large, the asymmetric losses introduced by the filter can significantly reduce the amount of entanglement.

In theory, the use of identical waveguides should ensure a perfect overlap of the spatial modes of the generated photons. In practice, however, the production process often introduces small variations between identically designed waveguides. In our case, the situation is complicated by the fact that the waveguides are made of different materials, have different dimensions and the signal and idler photons are at widely separated wavelengths. In short, these factors make a simple configuration with just a single interferometer, as depicted in figure 1, impossible for several reasons, in particular when only a single aspheric lens is used to collect the signal and idler photons at the output of the waveguides. Already for a single waveguide, the chromatic aberration of the lense does not allow for simultaneous collimation of the signal and idler beams. On top of that there is the more fundamental problem that the refractive index profiles of the waveguides depend on the chip and on the wavelength. The result is that the signal and idler spatial modes have different sizes and are not centered with respect to each other, even if generated in the same waveguide. For different waveguides, signal and idler beams can in general not be pairwise matched by even the most sophisticated lens system.
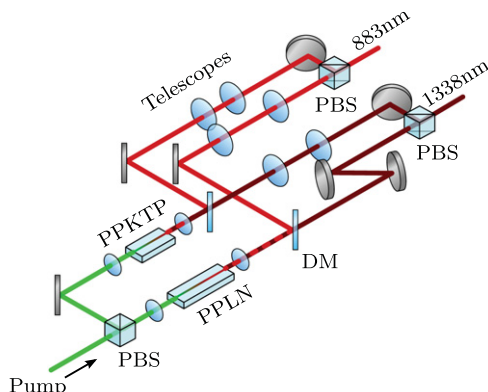
Figure 2. The spatial modes of the photons generated in different waveguides can be efficiently matched by using two interleaved interferometers with appropriate telescopes.

One way to properly match the spatial modes is to part ways with the idea of using a single interferometer and instead use two interleaved interferometers, as shown in figure 2. This gives control of all four spatial modes involved. A single uncoated achromatic lens (Thorlabs C220-TME) after each waveguide is positioned such that the idler beams are collimated. Right after that, dichroic mirrors separate signal and idler beams, leading to four individual beam paths. Telescopes in three of the paths adapt the spatial modes such that the signal and idler modes are separately matched to each other and to the single-mode fibers that will eventually receive the photons. Finally, the signal and idler modes are, respectively, recombined on two PBSs.

4.3. Relative phase

The relative phase from equation (1) has contributions from signal and idler photons, $\phi = \phi_s(\omega_s) + \phi_i(\omega_i)$, and depends, in general, on the frequencies ω_s and ω_i of the signal and idler photons, respectively. In turn, ϕ_s is the difference phase acquired between the horizontal and vertical paths of the respective interferometer, and similarly for the idler photon. To obtain a high degree of entanglement, it is important that ϕ is well-defined for all frequencies within the final bandwidth of the photons. Hence, the path length difference ΔL_x ($x =$ s, i) for the two interferometers should be much smaller than the coherence length of the photons after spectral filtering. For the estimation of ΔL_x one should not forget the dispersion inside the waveguides and that also the propagation of the pump light up to the waveguides is important.

In the experiment we actively stabilize ϕ. For this purpose, each interferometer contains a mirror mounted on a piezo-electric transducer. We use the pump light at 532 nm that is transmitted through the waveguides and leaks into all parts of the interferometer to continuously probe the phase. The PBSs at the input and outputs of the interferometers are not perfect at this wavelength, such that residual interference can be seen on the intensity variations picked up by two photodiodes. Note that, in general, the pump light transmitted through the horizontal and vertical paths of the interferometers will not have the same intensity. Additionally, the coating on the end face of the PPLN chip, the reliance on imperfections and the bad spatial mode-matching of the 532 nm light at the output result in peak-to-peak intensity variations as low as a few 10 nW. Using a lock-in technique, an error signal can nevertheless be extracted and used to stabilize the phases of the interferometers.

Using this technique, the stabilization works reliably for a typical duration of 5–10 h, a duration after which the thermal drift in the laboratory would typically exceed the compensation range of the piezos. However, the technique has two limitations to keep in mind. First, the absolute value of the phase can not be chosen at will and is more or less random for every activation of the lock. Second, since the 532 nm light follows a slightly different path than the signal and idler photons, and the temperature dependence of the refractive index inside the waveguides is wavelength dependent, differential phase shifts can appear. In practice, we observe residual phase drifts on the order of 1° per hour, as determined by repeatedly applying the measurement procedure described in section 7.

4.4. Spectral filtering

In experiments where one of the photons in a pair is coupled to a narrowband receiver, such as an atomic ensemble, spectral filtering is essential. In the typical scenario of SPDC with a narrowband pump laser, energy conservation ensures that a detection of, say, the idler photon after a suitable spectral filter guarantees that the signal photon is within the target spectral range. At first glance such one-sided filtering might seem entirely sufficient. In practice, however, and in particular in the case of strong filtering, multi-pair production can add a significant background of signal photons outside the desired bandwidth, which leads to a reduction of the signal-to-noise ratio of coincidence detections. Hence, also the signal photon needs to be filtered at least to some extent.

Efficiency, stability and ease of use are typical criteria for choosing suitable spectral filters. For a given bandwidth, one wants to use as few filtering elements as possible, as all of them are bound to introduce photon loss and have stabilization requirements. The case of polarization-entangled photon pairs adds the concern that both the spectrum and the efficiency of the filters need to be independent of polarization. This precludes the use of traditional techniques such as diffraction gratings, but also of some more recent developments such as phase-shifted fiber Bragg gratings and Fabry–Perot cavities based on coated lenses [35].

The spectra of the two waveguides were measured using custom-built spectrometers based on diffraction gratings and single-photon-sensitive CCD cameras; see figure 3. The spectrometers have an estimated resolution on the order of 200 GHz full width at half maximum (FWHM) at 883 nm and 100 GHz at 1338 nm. Gaussian fits to the respective signal and idler spectra serve to estimate the phasematching bandwidth. For the PPKTP waveguide the two fits approximately agree, yielding a FWHM of 791(28) GHz for the signal and 724(39) GHz for the idler. The signal photons generated in the PPLN waveguide are measured to be 443(12) GHz wide, and the idler photons 328(11) GHz. While both values may be resolution limited, the discrepancy is most likely due to the inferior resolution at 883 nm.

Assuming the sinc^2-shaped spectrum of ideal SPDC and neglecting the dispersion caused by the refractive index profile of the waveguide, we can use Sellmeier equations for KTP [36] and $LiNbO_3$ [37] to find a theoretical estimate of the bandwidths (see appendix A). For the waveguide from AdvR the FWHM is estimated to 540 GHz, while for the guide from Paderborn we find 100 GHz. In both cases, the measured bandwidths are larger. Apart from the limited resolution of the spectrometer, we attribute this deviation to inhomogeneities of the waveguide structure over the interaction length, which also explains why the measured spectra do not exhibit a sinc^2 shape. Finally, propagation losses of the pump laser in the waveguide can lead to a reduced effective interaction length and hence a broadening of the spectra.
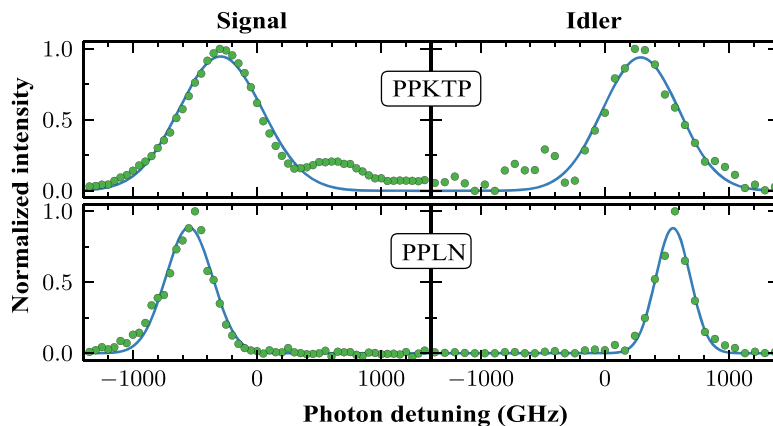
Figure 3. Non-filtered spectra of the photons generated by the two waveguides. Detunings are given with respect to a reference laser at 883.2 nm for the signal photon, and for the idler with respect to light from difference-frequency generation using the same laser. Gaussian fits (solid lines) give estimates of the spectral bandwidths (see text). For these plots, the temperature of the waveguides had not yet been properly adjusted.

We shall now describe the filtering system used to reduce the spectral width of the photon pairs to 240 MHz FWHM. We use two-sided filtering, that is, filters are applied to both the signal and idler photons. At first glance, it would seem that one-sided filtering is sufficient, because energy conservation dictates that the two photons in a pair created by a narrowband pump laser have the same bandwidth, if detected in coincidence. However, accidental coincidences stemming from different pairs do not have this restriction, such that the cross-correlations for one-sided filtering are strongly reduced. This reduction is typically much stronger than the increase in the pair detection rate (corrected for accidental coincidences) gained by one-sided filtering. A quantitative comparison between one-sided and two-sided filtering is given in appendix C.

The filtering for the signal and idler photons is very similar and is done in two steps. The signal photon is first sent onto a volume Bragg grating (VBG) made by Optigrate. The VBG has a nominal diffraction efficiency of 98.6%, although the value in the experiment is ≈90%. The spectral selectivity is specified to 54 GHz at FWHM. Grating parameters are such that the diffracted beam forms an angle of about 7° with the incoming beam. We have not seen any polarization dependence of significance in the performance of the VBG. The second filtering step is an air-spaced Fabry–Perot etalon made by SLS Optics Ltd. The etalon has a line width of $\Gamma_s/(2\pi) = 600$ MHz and a free spectral range (FSR) of 50 GHz, corresponding to a finesse of 83. The peak transmission of the etalon is about 80%.

For the idler photon, the first filter is a custom-made Fabry–Perot cavity with line width $\Gamma_i/(2\pi) = 240$ MHz and an FSR of 60 GHz, corresponding to a finesse of 250. By itself, we achieved peak transmissions through the cavity exceeding 80%. Integrated in the setup of the photon pair source, mode matching was slightly worse, giving a typical transmission around 60%. The cavity was followed by a VBG with a FWHM diffraction window of 27 GHz and nominal efficiency of 99.6%. In this case, experimental observations were compatible with specifications.

The idea behind the combination of Fabry–Perot filter and VBG is to select only a single longitudinal mode of the cavity or the etalon. In practice, however, a typical reflection spectrum of a VBG can have significant side lobes [38]. From the measured second-order auto-correlation functions (see section 5), we estimate that more than 70% of the transmitted signal photons and more than 95% of the idler photons belong to the desired longitudinal mode.

One issue with narrowband filters is the spectral stability. Long-term stability for the VBGs is easily achieved by using a stable mechanical mount, as they have practically no sensitivity to temperature fluctuations. The Fabry–Perot filters are stabilized in temperature, but exhibit residual drifts on the order of 100 MHz per hour. If the center frequencies of the signal and idler filters drift such that they no longer add up to the frequency of the pump laser, the coincidence rate will drop. We compensate this by using a reference laser at 883 nm, which may be stabilized to the etalon, for difference frequency generation (DFG) in the PPLN waveguide, effectively giving coherent light at the idler frequency. The frequency of the pump laser is then adjusted to optimize the transmission of the DFG light through the cavity. During experiments, we switch between DFG and SPDC every few tens of milliseconds, and the transmitted DFG light is detected with single-photon detectors and integrated over approximately 1 s. The stabilization was implemented in software for previous work [23–25], and reliably compensates the slow and weak thermal drifts. This technique also provides a means for active stabilization to the Nd:YSO quantum memory: tuning the 883 nm reference laser to the relevant transition ensures that the photon pairs are simultaneously in resonance with the idler cavity and the quantum memory.

An advantage of the direct filtering approach to generate narrowband photon pairs is the low sensitivity to fluctuations of the temperature of the waveguides themselves. Techniques based on OPO are much more sensitive [18, 20, 21]. In our case, temperature fluctuations shift the phase-matching spectrum as a whole. Since the frequency filters post-select a very small part of the whole spectrum, these variations can be tolerated as long as the shift is small compared to the phase-matching bandwidth, such that the pair-creation rate at the position of the filters remains approximately constant. We measured a temperature-dependent shift of the phase-matching spectrum of $280\,\mathrm{GHz\,K^{-1}}$ and $190\,\mathrm{GHz\,K^{-1}}$ for the PPLN and PPKTP waveguides, respectively. Requiring that the spectra shift less than, say, 5% of their width corresponds to a temperature stability below $0.05\,\mathrm{K}$ and $0.2\,\mathrm{K}$, respectively, which is routinely achieved also in the long term.

5. Spectral characterization via correlation functions

Correlation functions are a useful tool for the characterization of light sources. We consider, in particular, the normalized second-order correlation functions, which are unaffected by photon loss or detector inefficiency. They are defined as

$$g_{jk}^{(2)}(\tau) \equiv \frac{\left\langle E_j^\dagger(t) E_k^\dagger(t+\tau) E_k(t+\tau) E_j(t) \right\rangle}{\left\langle E_j^\dagger(t) E_j(t) \right\rangle \left\langle E_k^\dagger(t+\tau) E_k(t+\tau) \right\rangle}, \tag{2}$$

where the indices $j, k \in \{\mathrm{s, i}\}$ represent the signal or idler photon, respectively. A measurement of $g_{jk}^{(2)}(\tau)$ consists of first determining the rate of coincidence detections between modes j and k at a time delay τ. This is effectively a measurement of the non-normalized

second-order coherence function, which is the numerator in equation (2). The normalization is then performed with respect to the rate of coincidences between photons from uncorrelated pairs created at times differing by much more than the coherence time of the photons.

By itself, the second-order cross-correlation function $g_{si}^{(2)}(\tau)$ gives a measure of the quality of a photon-pair source, because noise photons stemming from imperfect spectral filtering or fluorescence generated in the down-conversion crystal inevitably reduce the amount of correlations. The auto-correlation functions $g_{ss}^{(2)}(\tau)$ and $g_{ii}^{(2)}(\tau)$ give information about the multimode character of the photons and their spectra. Finally, the cross- and auto-correlation functions can be combined in a Cauchy–Schwarz inequality whose violation proves the quantum character of the photon-pair source [39].

In this section we look at the normalized auto- and cross-correlation functions of the signal and idler photons. We show that the shape of the correlation functions is exactly as one would expect from the spectral filtering, if the jitter of the detectors is taken properly into account. Additionally, we use the auto-correlation functions to deduce the probability that a detected signal (or idler) photon stems from the desired mode of the filtering etalon (or cavity).

5.1. Correlation functions

The spectral filtering reduces the uncertainty in energy of the signal and idler photons. The effect can be directly seen on the normalized second-order auto- and cross-correlation functions, for which simple analytical expressions can be derived for collinear, low-gain, SPDC with plane-wave fields. The detailed derivation is given in appendix B. In brief, it procedes as follows. First, expressions for the first-order field correlation functions without filtering can be obtained via the Bogoliubov transformation that describes the input–output relation of the SPDC process [40, 41]. Next, spectral filtering is included through the convolution of the correlation functions with the filter impulse response [42]. In the case where the bandwidth of the filters is much smaller than the bandwidth of the SPDC process, the temporal dependence of the correlation functions is entirely given by the spectral filtering. Finally, higher-order correlation functions are obtained by applying the quantum form of the Gaussian moment-factoring theorem [40]. We arrive at the following expressions for the normalized second-order cross- and auto-correlation functions for Lorentzian-shaped spectral filters

$$g_{si}^{(2)}(\tau) = 1 + 4\frac{B}{R}\frac{\Gamma_s \Gamma_i}{(\Gamma_s + \Gamma_i)^2} f_{si}(\tau),$$

$$g_{ss}^{(2)}(\tau) = 1 + f_{ss}(\tau),$$

$$g_{ii}^{(2)}(\tau) = 1 + f_{ii}(\tau),\tag{3}$$

where the temporal dependence is given by

$$f_{jk}(\tau) = \begin{cases} e^{\Gamma_j \tau} & \text{for } \tau < 0 \\ e^{-\Gamma_k \tau} & \text{for } \tau \geqslant 0 \end{cases}.\tag{4}$$

The cross-correlation function depends on the inverse of the ratio of the R/B. Here, B is the phase-matching bandwidth and R is the rate of photon pair creation. Hence, $1/B$ is seen as the duration of one temporal mode. The low-gain limit of the source is obtained with the probability to create a pair per temporal mode is much smaller than one, i.e. $R/B \ll 1$. In this regime, the
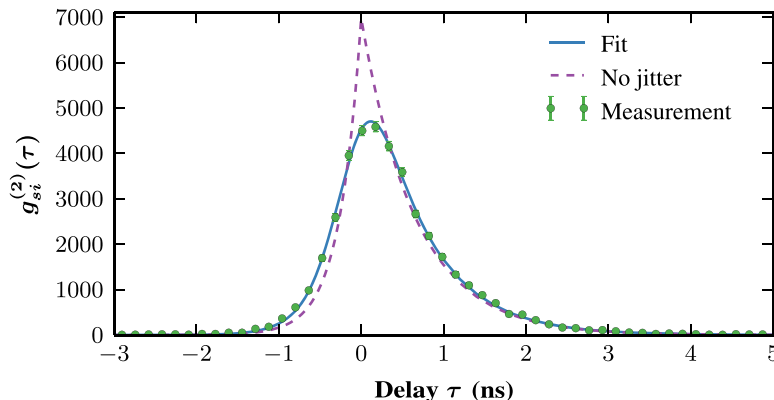
Figure 4. Example of a cross-correlation function measured for the PPKTP waveguide using a binning of 162 ps. The solid line is a fit to the theoretical line shape (equation (3)), corrected for detector jitter, where the only free parameters are the ratio R/B and a horizontal offset. The dashed line is the cross-correlation that we could have obtained with a jitter-free detection system.

rate R is proportional to the pump power. Additionally, the cross-correlation depends on the ratio of the filter bandwidths. For a given value of R/B, a larger mismatch makes it more likely that only one of the photons in a pair passes the filters, which leads to a reduction of the cross-correlation.

5.2. Detector jitter

Figure 4 shows an example of a measured cross-correlation function for the PPKTP waveguide. The combination of detectors, a Perkin–Elmer SPCM-AQRH-13 silicon avalanche photo diode and a super-conducting nanowire single-photon detector (SNSPD), had negligible dark count rates. To compare the measured temporal dependence with theory, the jitter of the detection system has to be taken into account. This can be done by convoluting the expression in equation (4) with the distribution function of the jitter. In our case the jitter is well modeled by a normal distribution, and the expression for the refined temporal dependence $\tilde{f}_{jk}(\tau)$ is given in the appendix. After this modification, we find excellent agreement between the measurement and a theoretical fit, where the only free parameters are a horizontal offset and the ratio R/B. Note that the jitter of $\sigma = 250$ ps for this combination of detectors reduces the maximum cross-correlation by a factor $\tilde{f}_{\mathrm{si}}(0) = 0.65$.

5.3. Multimode properties

Contrary to the cross-correlation function, the normalized auto-correlation functions do not depend on the spectral brightness. Instead, they reach a maximum value of $g_{jj}^{(2)}(0) = 2$, which reveals the thermal nature of the individual signal and idler fields.

A comparison between theory and experiment for the auto-correlation function of the idler photons generated in the PPKTP waveguide is plotted in figure 5. Detector jitter has been included as before by using $\tilde{f}_{\mathrm{ii}}(\tau)$ instead of $f_{\mathrm{ii}}(\tau)$. The detectors were a pair of SNSPDs with $\sigma = 125$ ps. The theoretical prediction is in excellent agreement with the measured data.
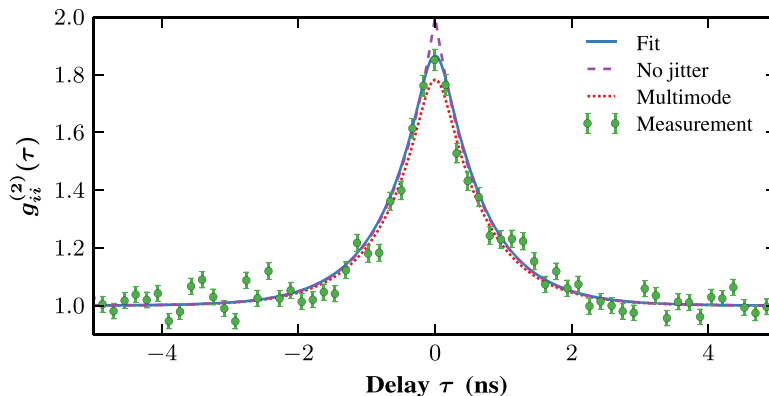
Figure 5. The second-order auto-correlation function of the idler photons generated in the PPKTP waveguide. Bins are 162 ps. The solid line is a fit to the theoretical line shape (equation (3) with jitter included), where the only free parameter is a horizontal offset. The dashed line is the auto-correlation that we could have obtained with a jitter-free detection system. The dotted line is a simulation corresponding to a 2.5% occupation of each nearest-neighbor longitudinal cavity mode.

A measurement of the second-order auto-correlation function allows, additionally, to characterize the presence of spurios spectral modes, that is, undesired modes of the Fabry–Perot filters, in the signal and idler fields. This has first been shown for pulsed and broadband SPDC in [43], where a set of orthogonal spectral modes is obtained via Schmidt decomposition of the joint-spectral amplitude of the signal and idler fields. By normalizing the occupation probabilities p_n of these modes such that $\sum p_n = 1$, the authors define an effective number of modes $K = 1 / \sum p_n^2$. This number, also known as the Schmidt number, quantifies the amount of spectral entanglement and is the reciprocal of the purity of the reduced states of the signal and idler modes [44]. Furthermore, it is shown in [43] that the inability to resolve these spectral modes results in a reduction of the auto-correlation functions, given by $g_{jj}^{(2)}(0) = 1 + 1/K$. Hence, a measurement of $g_{jj}^{(2)}(0)$ allows to directly determine K.

For continuous-wave SPDC subjected to narrow-band Fabry–Perot filters, the longitudinal modes of the filter form a suitable basis for the spectral decomposition. We define p_0 as the probability to find the photon in the desired longitudinal mode, and let p_n be the nth red-detuned (or blue-detuned) mode for $n > 0$ (or $n < 0$). We would like to determine a lower bound on p_0 via a measurement of the auto-correlation function. As in the case of pulsed SPDC, the presence of spurious longitudinal modes of the Fabry–Perot filter reduces the auto-correlation function. This is easily seen from the fact that $f_{jj}(\tau)$ is proportional to the absolute square of the Fourier transform of the power spectral density of the cavity transfer function (see also equations (B.6) and (B.8)). The presence of multiple longitudinal cavity modes will hence lead to oscillations of $g_{jj}^{(2)}(\tau)$ at a frequency corresponding to the FSR of the filter. If the detectors do not resolve these oscillations, they will be averaged out, leading to a reduction of $g_{jj}^{(2)}(\tau)$. However, in our case the detector jitter is sufficiently strong to give a reduction of the $g_{jj}^{(2)}(0)$ even for the single-mode case. To more clearly separate the contributions from detector jitter and spurious modes, we rewrite the auto-correlation function of equation (2) as
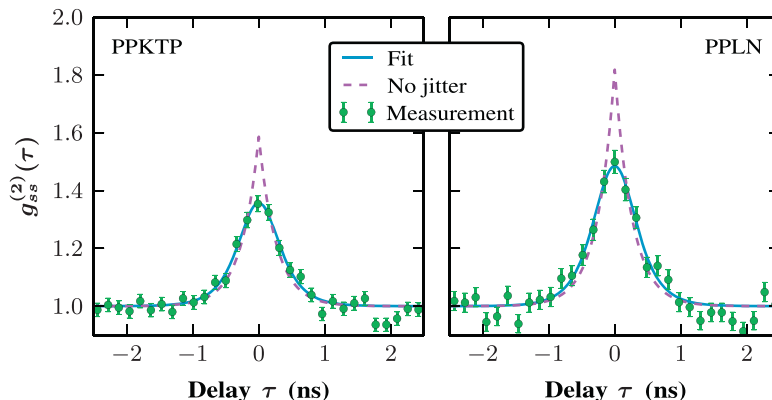
Figure 6. The second-order auto-correlation function of the signal photons generated in the PPKTP (left) and PPLN (right) waveguides. Spurious etalon modes prevent the peak from reaching a value of 2, even after the correction for detector jitter. Bins are 162 ps.

$$g_{jj}^{(2)}(\tau) = 1 + \frac{1}{K}\tilde{f}_{jj}(\tau), \tag{5}$$

where jitter has been taken into account explicitly via the use of $\tilde{f}_{jj}(\tau)$.

For the idler photon, the red dotted line in figure 5 shows the case of $p_0 = 0.95$ for the central cavity mode and $p_{\pm 1} = 0.025$ for the neighboring red- or blue-detuned modes, giving $K = 1.1$. The mismatch with the experimental data at zero delay is consistent with the selection of a single cavity mode by the filtering system.

The situation is different for the signal photon, for which auto-correlation measurements are shown in figure 6. Here, the bandwidth of the VBG is comparable to the FSR of the etalon, and contributions from spurious modes are to be expected. From a fit of equation (5) to the data, with K and σ as free parameters, we obtain $K = 1.71(8)$ for the PPKTP waveguide and $K = 1.22(6)$ for the PPLN waveguide. Assuming the worst case of only a total of two etalon modes with non-zero population, this corresponds to probabilities of $p_0 = 0.71(3)$ and $p_0 = 0.90(3)$, respectively, for the photon being in the desired etalon mode. We attribute the larger value of K for the PPKTP waveguide to the larger phase-matching bandwidth.

6. Efficiency characterization of the filtered photon sources

In this section we show a characterization of the individual performances of the two waveguides, including spectral filtering. The characterization aims at determining the spectral brightness and the collection and detection efficiencies of the photons. It consists of measuring as a function of the pump power the detection rates of signal and idler photons. Furthermore, we measured the photon-pair rate, that is, the signal-idler coincidence rate, corrected for accidental coincidences, for a coincidence window that is large compared to the coherence time. Finally, we also determined the power-dependence of the second-order cross-correlation function $g_{si}^{(2)}(\tau)$ at delay $\tau = 0$. The results are shown in figure 7.

For comparison to a theoretical model, we use the same derivation as for the correlation functions in the previous section. However, in the previous section the dark counts of the detectors were negligible. Dark counts add an offset to the signal and idler detection rates. Additionally, they give rise to accidental coincidences, which set an upper bound on the
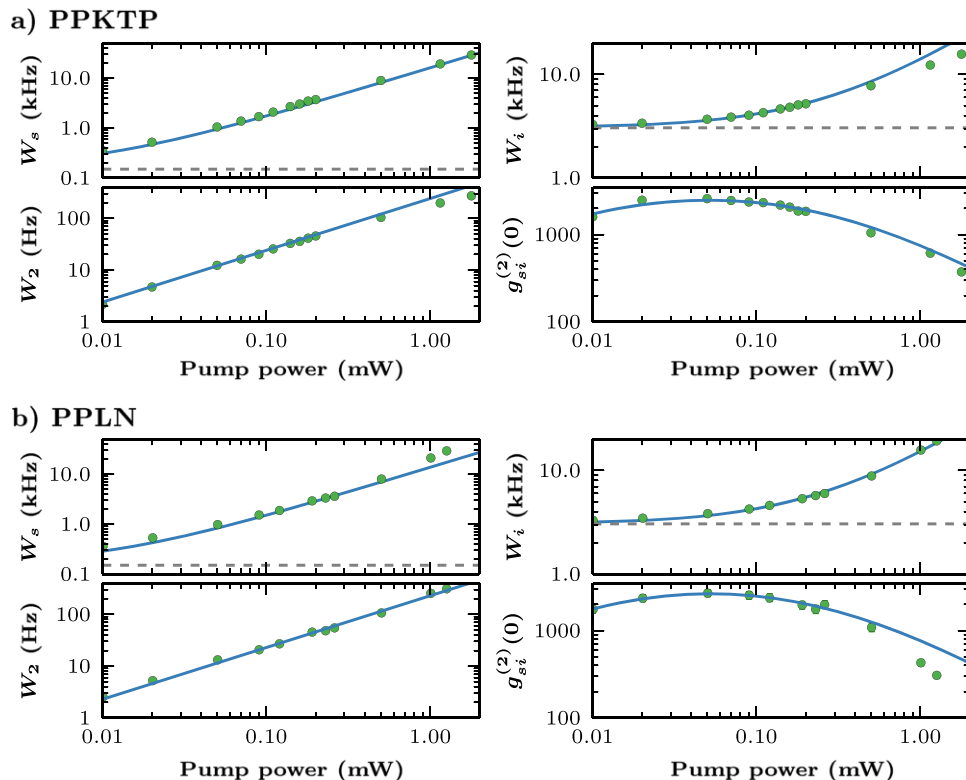
Figure 7. Characterization of (a) the PPKTP and (b) the PPLN waveguide. For each waveguide, the signal, idler and pair detection rates are plotted, as well as the value of the cross-correlation function at $\tau = 0$ delay. The dashed horizontal lines in the panels for the signal and idler rates indicate the detector noise level. For the measurement of the pair rate, a coincidence window of 6 ns was used, which is sufficiently large to encompass the entire coincidence peak (see figure 4). Additionally, accidental coincidences have been subtracted. The values of the cross-correlation function are based on a binning of 162 ps. A common fit (solid lines) to all four data sets for each waveguide was used to extract the spectral brightness and collection efficiencies (see also table 2).

normalized cross-correlation function at low pump powers. We included the dark count rate D_j in the model and also added finite detection efficiencies η_j to end up with the following set of equations (see also appendix B),

$$W_s = \frac{1}{4} \frac{\eta_s}{p_0} \frac{R}{B} \Gamma_s + D_s,$$

$$W_i = \frac{1}{4} \eta_i \frac{R}{B} \Gamma_i + D_i,$$

$$W_2 = \frac{1}{4} \eta_s \eta_i \frac{R}{B} \frac{\Gamma_s \Gamma_i}{\Gamma_s + \Gamma_i},$$

$$g_{si}^{(2)}(0) = 1 + \frac{1}{4} \frac{\tilde{f}_{si}(0) \eta_s \eta_i}{W_s W_i} \frac{R}{B} \left(\frac{\Gamma_s \Gamma_i}{\Gamma_s + \Gamma_i} \right)^2. \tag{6}$$

Table 2. Parameters as extracted from fitting the data in figure 7 to equations (6). $2\pi\,R/B$ is the spectral brightness, given in conventional units, for a pump power of 1 mW. η_s (or η_i) is the overall collection and detection efficiency for the signal (or idler) photon.

	Waveguide	
	PPKTP	PPLN
$2\pi\,R/B$	$2.45\,(6) \times 10^3\,(\text{s MHz})^{-1}$	$3.08\,(6) \times 10^3\,(\text{s MHz})^{-1}$
η_s	$3.1(2)\%$	$2.6(2)\%$
η_i	$7.4(1)\%$	$6.6(1)\%$

Here, the signal and idler rates W_s and W_i are essentially given by the spectral brightness of the waveguide times the respective bandwidth of the filtering system and attenuated by the detection efficiency. Since R is proportional to the pump power, so are W_s and W_i. W_s has also been corrected for the contribution of spurious etalon modes, which will increase the detection rate by a factor $1/p_0$. The behavior of the pair rate W_2 is similar, except that the photon pairs have an effective bandwidth of $\Gamma_s\Gamma_i/(\Gamma_s + \Gamma_i)$, which is smaller than the bandwidth of the signal and idler photons individually. Note that the measurement of W_2 includes correction for accidental coincidences, and no correction for dark counts needs to be applied to the theory. Finally, the expression for $g_{si}^{(2)}(0)$ is equivalent to the one given in equation (3), but the inclusion of dark counts prevents further simplification.

We used commercially available detectors for the measurements presented in figure 7. The signal detector by Perkin–Elmer has a dark-count rate of 150 Hz and a detection efficiency of about 30% at 880 nm. As detector for the idler photon served an ID220 by Id Quantique with 20% efficiency. To reduce the contribution of afterpulsing, the dead time of this detector was set to $20\,\mu$s, and we observed a dark-count rate of 3.0 kHz. The offset on the signal and idler count rates given by the dark counts is indicated by dashed lines in the top panels of figure 7.

A simultaneous fit to the equations (6) reproduces the measurements to a high extent. The free parameters in the fit are the spectral brightness R/B and the overall collection and detection efficiencies η_s and η_i. The results of the fit are shown in table 2. For the PPKTP waveguide the idler rate shows a negative deviation from the expected behavior at pump powers above 1 mW, where the detector starts being saturated. For the PPLN waveguide the saturation seems to be compensated by a higher pair-creation efficiency, indicated by a positive deviation of the signal rate and a significant drop in the cross-correlation.

In terms of the spectral brightness, the two waveguides perform on a similar level. We note however, that the specified pump power is measured in front of the waveguide. For both waveguides we estimate a coupling of the pump laser into the waveguide between 40–50%. Of this, only a fraction is coupled into the fundamental spatial mode, and hence contributing to SPDC. In principle, we would expect a higher brightness for the waveguide from Paderborn, since it is longer and PPLN has a larger nonlinear coefficient than PPKTP. The reason that we observe something different could be a non-optimal temperature of this waveguide in this measurement, which shifts the perfect phase matching slightly away from the filter transmission maximum. We also note that at pump powers above a few milliwatts, the operation of the PPLN waveguide is impaired by photorefraction, which leads to strong fluctuations of the spatial mode of the pump laser inside the waveguide.

In our experiments we are rarely constrained by the available pump laser power, and the spectral brightness is only of minor importance. More important are the achievable coincidence rates and the correlations between signal and idler photons. The coincidence rate is proportional to the product of the signal and idler collection and detection efficiencies, η_s and η_i. Also here we see similar values for the two waveguides, indicating a spatial mode-matching better than 80% for the signal photon and around 90% for the idler. The expected peak transmission for the signal path is $\eta_s \approx 3.6\%$ with contributions from a long-pass filter that removes the pump light (80%), the VBG (90%), the etalon (80%), fiber coupling (60%) and detector efficiency (30%). Additionally, the setup was already prepared for storage and retrieval in the quantum memory, adding losses due to a fiber-optical switch (70%), fiber connectors (70%) and another fiber coupling (70%). On the idler side, we expect $\eta_i \approx 8\%$, distributed over the cavity (60%), fiber coupling (70%) and detector efficiency (20%). The measured value for η_s and η_i, given in table 2, corresponds quite well to the expected values. We attribute the small differences to loss inside and at the end facets of the waveguides.

The measured cross-correlation function reaches for both waveguides a peak value of approximately 2600 at a pump power of $50\,\mu\text{W}$. At lower pump power correlations are reduced by dark counts, at higher pump powers by multi-pair emission.

7. Entanglement

The characterization of the two waveguides showed that a very high degree of mode-matching for the photons originating from the two waveguides has been obtained. Additionally, the spectral brightness is about the same. This means that it should be possible to achieve a high degree of entanglement by setting the pump polarization to an approximately equal superposition of horizontal and vertical, such that similar amounts of light arrive at the two waveguides. In practice, we neglect the small differences in coupling efficiencies and adjust the pump polarization such that the rate of coincidences from the two waveguides is about the same. It remains to be shown that the horizontally and vertically polarized photon pairs form a coherent superposition with a stable phase, which corresponds to an entangled state between the two photons.

Let us, for simplicity, assume that the photon pairs are produced in the maximally entangled state

$$\frac{1}{\sqrt{2}}\Big(|HH\rangle + e^{i\phi}\,|VV\rangle\Big). \tag{7}$$

A measurement that verifies the coherent nature of this state is illustrated in figure 8(a). First, the idler photon is measured in the basis $|\pm\rangle = (|H\rangle \pm |V\rangle)/\sqrt{2}$ using a half-wave plate and a PBS. If a photon is detected in the port of the beam splitter corresponding to, say, $|+\rangle$, the signal photon is projected onto the state $|\phi_+\rangle = (|H\rangle + e^{i\phi}\,|V\rangle)/\sqrt{2}$. Sending this through a quarter-wave plate and a half-wave plate whose fast axes are at angles of $\pi/4$ and θ to horizontal, respectively, transforms the signal photon into the linearly polarized state $|\beta\rangle = \sin\beta\,|H\rangle - \cos\beta\,|V\rangle$ with $\beta = 2\theta + \phi/2 + \pi/4$. We hence expect that the probability of detecting the signal photon after a PBS shows sinusoidal fringes as a function of θ with a period of $\pi/2$. The phase of the fringes depends on the phase ϕ of the initial entangled state (7), such that this kind of measurement can be used to determine ϕ. If, instead, the photon pairs are generated in a maximally mixed state $(|HH\rangle\langle HH| + |VV\rangle\langle VV|)/2$, the same measurement of
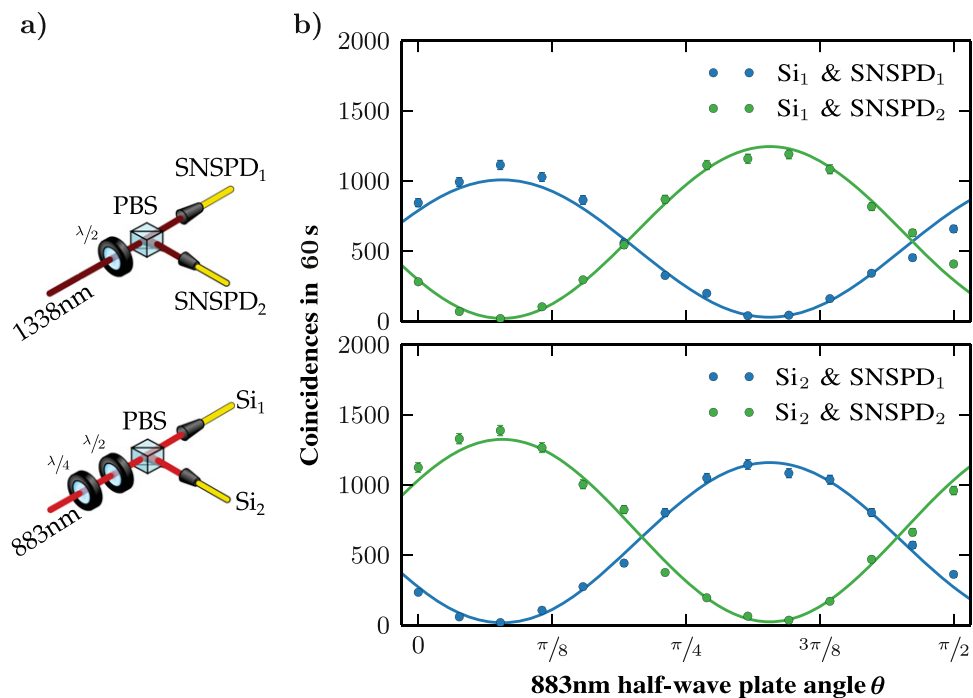
Figure 8. Characterization of the coherence of the pair source. (a) The idler photons are measured in the bases of diagonal polarization. This projects the signal photon onto a coherent superposition of $|H\rangle$ and $|V\rangle$ with unknown relative phase. A quarter-wave plate at fixed angle transforms this state into a linear polarization, which is analyzed with the help of a half-wave plate and a polarizing beam splitter. (b) Corresponding coincidence measurement for a coincidence window of 2 ns for the four detector combinations. Solid lines are sinusoidal fits with a fixed period and common phase. The fits yield an average visibility of $V = 96.1(9)\%$.

the coincidence rate will not show any dependence on θ. A fringe visibility larger than 33% is necessary to infer the presence of entanglement [45].

In figure 8(b) we show the outcome of the described measurement procedure. A pair of SNSPDs has been used for the idler photon, and Si avalanche photo diodes (Perkin–Elmer) for the signal photon. For each value of θ the number of coincidences in a 2 ns window have been integrated over a duration of 60 s for each of the four possibly detector combinations. The number of measured coincidences oscillates as a function of θ, as expected. A sinusoidal fit reveals an average visibility $V = 96.1(9)\%$, which indicates that the source generates photon pairs that are close to maximally entangled in polarization.

To unequivocally prove the presence of entanglement we performed a violation of the Clauser–Horne–Shimony–Holt (CHSH) inequality [46]. A quarter-wave plate was added to the polarization analysis of the idler photon, such that the setups for signal and idler photon of figure 8(a) were now identical. Additionally, the SNSPDs were replaced by ID220s for their higher detection efficiency. The wave plate allows to switch the measurement basis of the idler photon between $|\pm\rangle$ and the circular polarizations $(|H\rangle \pm \mathrm{i}\,|V\rangle)/\sqrt{2}$ by a rotation of the half-wave plate. These two basis sets were used for the measurement. Since we do not *a priori* know the relative phase ϕ of the photon pairs, we determine the optimal settings for the signal analyzer as follows. We set the idler analyzer to $|\pm\rangle$ and perform another measurement of the

type of figure 8 to determine the angle θ_{max} of the half-wave plate of the signal analyzer that gives a maximum between detectors Si_1 and $\mathrm{ID220}_1$. For the violation of the CHSH inequality we then use the angles $\theta_{\mathrm{max}} \pm \pi/16$. For an acquisition time of 5 min per setting we find a CHSH parameter of $S = 2.708(9)$, which is almost 80 standard deviations above the bound for separable states of $S \leqslant 2$.

8. Summary and outlook

We have presented a source of polarization-entangled photon pairs based on the nonlinear waveguides of different materials embedded in the arms of a polarization interferometer. We have shown that the source emits photon pairs with a high degree of entanglement and is compatible with the storage of one of the photons in a quantum memory. The wavelength of the other photon is in a telecom window, which permits the low-loss transmission over optical fiber. This combination makes the source particularly useful for quantum communication experiments.

Even though the photon-pair source is conceptually simple, a higher degree of integration would be desirable. Recent work along this direction includes the integrated spatial separation of signal and idler photons using an on-chip wavelength-division multiplexer [47] and the direct generation of 150 MHz broad photon pairs using a monolithic waveguide resonator [21]. Both of these techniques were demonstrated with similar wavelengths as used in this work. In particular the latter could greatly simplify the efficient generation of narrowband photon pairs, provided that the intrinsic resonator loss can be reduced. If this could further be combined with the on-chip generation of polarization-entangled photons using an interlaced bi-periodic structure [48], one would have the equivalent of the whole setup of figure 2 on a single chip, including spectral filtering. Together with the recent progress in solid-state quantum memories, these are promising perspectives for the development of compact and practical nodes for quantum communication.

Acknowledgments

Appendix A. Estimation of phase-matching bandwidth

The frequency dependence of SPDC is given by the joint spectral amplitude $f(\omega_{\mathrm{s}}, \omega_{\mathrm{i}})$, which can be written as the product of two functions,

$$f(\omega_{\mathrm{s}}, \omega_{\mathrm{i}}) = \alpha(\omega_{\mathrm{s}} + \omega_{\mathrm{i}})\Phi(\omega_{\mathrm{s}}, \omega_{\mathrm{i}}), \tag{A.1}$$

where ω_{s} (or ω_{i}) is the frequency of the signal (or idler) photon, $\alpha(\omega)$ represents the spectrum of the pump laser and $\Phi(\omega_{\mathrm{s}}, \omega_{\mathrm{i}}) = \mathrm{sinc}(\Delta kL/2)$ is the phase-matching function. The state of a single photon pair can be written in terms of the joint spectral amplitude as

$$|\Psi\rangle \propto \int_{-\infty}^{\infty} d\omega_s \int_{-\infty}^{\infty} d\omega_i \, f(\omega_s, \omega_i) a^{\dagger}(\omega_s) a^{\dagger}(\omega_i) |\text{vac}\rangle, \tag{A.2}$$

where $a^{\dagger}(\omega)$ is the photon creation operator at frequency ω. We recognize, that $f(\omega_s, \omega_i)$ is the spectral wavefunction of the photon pair. It follows that the spectral distribution, that is, the probability to find a photon in an infinitesimal interval at frequency ω, of the signal or idler photon is given by

$$S(\omega_s) \propto \left| \int_{-\infty}^{\infty} d\omega_i \, f(\omega_s, \omega_i) \right|^2$$

$$S(\omega_i) \propto \left| \int_{-\infty}^{\infty} d\omega_s \, f(\omega_s, \omega_i) \right|^2. \tag{A.3}$$

In the case of a highly coherent pump laser, $\alpha(\omega)$ can be approximated by a Dirac delta function, $\delta(\omega - \omega_p)$, and the spectra of the signal and idler photons is given by the phase matching, only, i.e.

$$S(\omega_j) \propto \text{sinc}^2(\Delta k L/2). \tag{A.4}$$

The phase mismatch is given by

$$\Delta k = 2\pi \left(\frac{n_p(\lambda_p)}{\lambda_p} - \frac{n_s(\lambda_s)}{\lambda_s} - \frac{n_i(\lambda_i)}{\lambda_i} - \frac{1}{\Lambda} \right), \tag{A.5}$$

with n_x and λ_x ($x = $ p, s, i) the refractive index and wavelength of pump, signal and idler photons, respectively. Λ is the period of poling. Here, as a first approximation, we have neglected the effect of the waveguide. A more accurate expression would use the propagation constants of the pump, signal and idler modes for the given waveguide refractive index profile.

　　We want to estimate the FWHM bandwidth of the photons generated by SPDC. To this end, we first remember that $\lambda_i = (\lambda_p^{-1} - \lambda_s^{-1})^{-1}$ due to energy conservation, such that the phase mismatch becomes a function of the signal wavelength only. For phase-matching $\Delta k = 0$, and the bandwidth is determined by the dispersion, which to first order is given by

$$\begin{aligned} \Delta k(\lambda) &\simeq \frac{d\Delta k(\lambda)}{d\nu} \Delta\nu = \frac{d\Delta k(\lambda)}{d\lambda} \frac{d\lambda}{d\nu} \Delta\nu \\ &= \frac{d\Delta k(\lambda)}{d\lambda} \frac{-\lambda^2}{c} \Delta\nu \\ &\equiv \Delta k' \Delta\nu. \end{aligned} \tag{A.6}$$

Note that the contributions of the pump wavelength and the periodic poling to $\Delta k(\lambda)$ are constant, so they will not affect $\Delta k'$. Using equation (A.6), the argument of the sinc^2 function in equation (A.4) becomes $x = \Delta k' \Delta\nu L/2$. Knowing that the sinc squared reaches half its maximum value at $x_{1/2} = 1.39156$, the FWHM bandwidh is given by

$$\Delta\nu_{\text{FWHM}} = \frac{4x_{1/2}}{|\Delta k'| L}. \tag{A.7}$$

Using the Sellmeier equations for KTP [36] and LiNbO$_3$ [37], we can calculate $\Delta k'$ and the resulting values for $\Delta\nu_{\text{FWHM}}$. These are given in table A1.

Table A1. Values for the estimation of the FWHM bandwidth of the two waveguides. For the PPLN waveguide we assume a temperature of 180 °C.

Waveguide	$\Delta k'$ ((mm GHz)$^{-1}$)	L (mm)	$\Delta\nu_{\text{FWHM (GHz)}}$
PPKTP	-7.93×10^{-4}	13	539
PPLN	-1.14×10^{-3}	50	97

Appendix B. Analytical model for SPDC with spectral filtering

We shall here give a brief derivation of the expressions for the signal and idler rates, the coincidence rate and the second-order correlation function of the waveguides, including the application of spectral filtering. As a starting point we will take the treatment presented by Razavi *et al* [40] (see also [41]), assuming collinear SPDC with plane-wave fields. Furthermore, the depletion of the pump and group-velocity dispersion have been neglected.

We start by giving expressions for the first-order correlation functions, from which one can calculate the event rates. With the help of the quantum form of the Gaussian moment-factoring theorem, all higher-order correlation functions can be derived [40].

B.1. First-order correlation functions

Defining scalar photon-units positive-frequency field operators

$$E_j(t) = \frac{1}{2\pi} \int_{-\infty}^{\infty} d\omega\, a(\omega) e^{-i\omega t}, \quad j = \text{s, i}, \tag{B.1}$$

where $a(\omega)$ is the photon annihilation operator in the frequency domain, Razavi *et al* use a Bogoliubov transformation to derive the following set of first-order correlation functions for the SPDC output state

$$\left\langle E_j^\dagger(t+\tau) E_j(t) \right\rangle = e^{i\omega_j\tau} \times C_{\text{auto}}(\tau),$$

$$\left\langle E_j(t+\tau) E_k(t) \right\rangle = \left(1 - \delta_{jk}\right) e^{-i\left(\omega_p t + \omega_j\tau\right)} \times C_{\text{cross}}(\tau), \tag{B.2}$$

where δ_{jk} is the Kronecker delta function and $j, k \in \{\text{s, i}\}$. In the low-gain regime of SPDC, the envelope functions $C_{\text{auto}}(\tau)$ and $C_{\text{cross}}(\tau)$ are given by

$$C_{\text{auto}}(\tau) = \begin{cases} R(1 - |\tau|\, B) & \text{for } |\tau|\, B \leqslant 1, \\ 0 & \text{otherwise} \end{cases},$$

$$C_{\text{cross}}(\tau) = \begin{cases} \sqrt{RB} & \text{for } |\tau|\, B \leqslant \frac{1}{2} \\ 0 & \text{otherwise} \end{cases}. \tag{B.3}$$

Here, R is the rate of photon pair creation and proportional to the pump power, and $B = 2\pi/(\Delta k' L)$ is proportional to the bandwidth. The ratio R/B is often termed the spectral brightness of the photon pair source.

When adding spectral filtering, the envelope functions get convoluted with the impulse response functions $F_j(t)$ of the filters [42]. For the autocorrelation,

$$C_{\text{auto}}^{(j)}(\tau) = \int_{-\infty}^{\infty} dt' \int_{-\infty}^{\infty} dt'' \, F_j^*(t + \tau - t') F_j(t - t'') \, C_{\text{auto}}(t' - t'')$$
$$\approx \alpha \int_{-\infty}^{\infty} dt' \, F_j^*(t + \tau - t') F_j(t - t'), \tag{B.4}$$

where we have taken $C_{\text{auto}}(t' - t'') \approx \alpha \, \delta(t' - t'')$, which is valid if the bandwidth of the filter is much smaller than B. The constant α is

$$\alpha = \int_{-\infty}^{\infty} dt' C_{\text{auto}}(t' - t'') = \frac{R}{B}. \tag{B.5}$$

We further consider a Lorentzian filter with FWHM Γ_j whose transfer and impulse response functions are given by

$$H_j(\omega) = \frac{\Gamma_j}{\Gamma_j - 2i\omega}, \tag{B.6}$$

$$F_j(\tau) = \frac{1}{2\pi} \int_{-\infty}^{\infty} d\omega \, H_j(\omega) e^{i\omega\tau}$$
$$= \frac{\Gamma_j}{2} \Theta(\tau) e^{-\Gamma_j \tau/2}, \tag{B.7}$$

where $\Theta(\tau)$ is the Heaviside step function. We then arrive at the final expression for the auto-correlation envelope

$$C_{\text{auto}}^{(j)}(\tau) = \frac{1}{4} \frac{R}{B} \Gamma_j e^{-\Gamma_j |\tau|/2}. \tag{B.8}$$

Performing a similar calculation for the cross-correlation envelope, we get

$$C_{\text{cross}}^{(jk)}(\tau) = \frac{1}{2} \sqrt{\frac{R}{B}} \frac{\Gamma_j \Gamma_k}{\Gamma_j + \Gamma_k} \times \begin{cases} e^{\Gamma_k \tau/2} & \text{for } \tau < 0 \\ e^{-\Gamma_j \tau/2} & \text{for } \tau \geqslant 0 \end{cases}. \tag{B.9}$$

Finally, let us introduce, for convenience, the signal and idler flux,

$$W_j \equiv C_{\text{auto}}^{(j)}(0) = \frac{1}{4} \frac{R}{B} \Gamma_j, \tag{B.10}$$

and the pair flux

$$W_2 \equiv \int_{-\infty}^{\infty} d\tau \, \left| C_{\text{cross}}^{(jk)}(\tau) \right|^2$$
$$= \frac{1}{4} \frac{R}{B} \frac{\Gamma_j \Gamma_k}{\Gamma_j + \Gamma_k}$$
$$= W_j \times \frac{\Gamma_k}{\Gamma_j + \Gamma_k}. \tag{B.11}$$

The last line of equation (B.11) says that the pair flux is equal to the flux if signal or idler rescaled by the probability that a photon that has already been projected onto the spectrum of one of the filters also passes the second filter. We note that this expression is valid only for perfectly correlated photon pairs and does not contain contributions from multi-pair emission. These will be included in the next section, where we consider second-order correlation functions.

B.2. Second-order correlation functions

The normalized second-order cross-correlation function is defined as

$$g_{\text{si}}^{(2)}(\tau) \equiv \frac{\left\langle E_{\text{s}}^{\dagger}(t)E_{\text{i}}^{\dagger}(t+\tau)E_{\text{i}}(t+\tau)E_{\text{s}}(t)\right\rangle}{\left\langle E_{\text{s}}^{\dagger}(t)E_{\text{s}}(t)\right\rangle\left\langle E_{\text{i}}^{\dagger}(t+\tau)E_{\text{i}}(t+\tau)\right\rangle}$$

$$= \frac{G_{\text{si}}^{(2)}(\tau)}{W_{\text{s}}\,W_{\text{i}}}, \tag{B.12}$$

where the numerator is the non-normalized second-order cross-correlation function. Applying the Gaussian moment-factoring theorem, it can be shown that

$$G_{\text{si}}^{(2)}(\tau) = W_{\text{s}}\,W_{\text{i}} + \left| C_{\text{cross}}^{(si)}(\tau)\right|^{2}, \tag{B.13}$$

where the first term is proportional to the coincidence rate that is expected for completely uncorrelated photons, often called accidental coincidences. Using equations (B.9) and (B.10), we find

$$g_{\text{si}}^{(2)}(\tau) = 1 + \frac{\left| C_{\text{cross}}^{(\text{si})}(\tau)\right|^{2}}{W_{\text{s}}W_{\text{i}}}$$

$$= 1 + 4\frac{B}{R}\frac{\Gamma_{\text{s}}\Gamma_{\text{i}}}{\left(\Gamma_{\text{s}}+\Gamma_{\text{i}}\right)^{2}} \times f_{\text{si}}(\tau)$$

$$f_{jk}(\tau) = \begin{cases} \mathrm{e}^{\Gamma_{j}\tau} & \text{for } \tau < 0 \\ \mathrm{e}^{-\Gamma_{k}\tau} & \text{for } \tau \geqslant 0 \end{cases}. \tag{B.14}$$

The derivation of the second-order auto-correlation functions for the signal and idler photons proceeds along the same lines as that of the cross-correlation. The auto-correlation function is defined as

$$g_{jj}^{(2)}(\tau) \equiv \frac{\left\langle E_{j}^{\dagger}(t)E_{j}^{\dagger}(t+\tau)E_{j}(t+\tau)E_{j}(t)\right\rangle}{\left\langle E_{j}^{\dagger}(t)E_{j}(t)\right\rangle\left\langle E_{j}^{\dagger}(t+\tau)E_{j}(t+\tau)\right\rangle}. \tag{B.15}$$

Applying the same steps as before, this can be shown to be equal to

$$g_{jj}^{(2)}(\tau) = 1 + \frac{\left| C_{\text{auto}}^{(j)}(\tau)\right|^{2}}{W_{j}^{2}} = 1 + f_{jj}(\tau), \tag{B.16}$$

where we have reused the definition of $f_{jk}(\tau)$ from equation (B.14).

B.3. Inclusion of experimental imperfections

Before the expressions derived in the appendices B.1 and B.2 can be compared to the experimental data, they need to be slightly modified to take into account experimental imperfections in the shape of finite efficiencies, dark counts and electronic jitter.

Let us start by considering the jitter of our detection system, which is well modeled by a normal distribution

$$j(t) = \frac{1}{\sqrt{2\pi\sigma^2}} e^{-t^2/(2\sigma^2)}. \tag{B.17}$$

The effect on the measured cross- and auto-correlation functions can be calculated as the convolution of $f_{jk}(\tau)$ from equation (B.14) with $j(t)$, and one obtains

$$\tilde{f}_{jk}(\tau) = \frac{1}{2}\left[e^{\Gamma_j\left(\Gamma_j\sigma^2/2 + t\right)} \operatorname{erfc}\left(\frac{\Gamma_j\,\sigma^2 + t}{\sqrt{2}\,\sigma}\right) + e^{\Gamma_k\left(\Gamma_k\sigma^2/2 - t\right)} \operatorname{erfc}\left(\frac{\Gamma_k\,\sigma^2 - t}{\sqrt{2}\,\sigma}\right)\right]. \tag{B.18}$$

The spectral filters do not have unit peak transmission. Additionally, the detectors have a finite efficiency and there is loss on the surfaces of optical elements and when coupling into single-mode fiber. By gathering all the losses into a single coefficient, they can be taken into account by adding a prefactor of $\sqrt{\eta_j}$ to the transfer function (B.6). This leads to a reduction of the signal and idler flux (B.10) by a factor of η_j, and the pair flux (B.11) is correspondingly reduced by a factor $\eta_j\eta_k$.

Besides the finite efficiency of the filtering, the etalon or cavity may not be well-approximated by a single Lorentzian filter. This is the case if more than one longitudinal mode is excited. Spurious modes contribute the photon flux and increase it by a factor $1/p_0$ where p_0 is fraction of the photons that end up in the desired mode. However, spurious modes cannot contribute to the pair flux, since the FSR of etalon and cavity are incommensurate. As explained in the main text, the signal filtering suffers from such spurious modes, and a correction has been added to the signal flux.

Detector dark counts add an offset to the detected photon flux and will also contribute to the accidental coincidences. This effect can be added to the formalism by introducing a constant term D_j to equation (B.10) and using equations (B.12) and (B.13) for comparison with the measurements, instead of the simplified expression (B.14). Please note that the pair flux W_2 by definition does not contain contributions from accidental coincidences. In summary, the experimental data presented in figure 7 has been fitted to the expressions

$$W_s = \frac{1}{4}\frac{\eta_s}{p_0}\frac{R}{B}\Gamma_s + D_s,$$

$$W_i = \frac{1}{4}\eta_i\frac{R}{B}\Gamma_i + D_i,$$

$$W_2 = \frac{1}{4}\eta_s\eta_i\frac{R}{B}\frac{\Gamma_s\Gamma_i}{\Gamma_s + \Gamma_i},$$

$$g_{si}^{(2)}(0) = 1 + \frac{1}{4}\frac{\tilde{f}_{si}(0)\eta_s\eta_i}{W_s W_i}\frac{R}{B}\left(\frac{\Gamma_s\Gamma_i}{\Gamma_s + \Gamma_i}\right)^2 \tag{B.19}$$

with the free parameters η_s, η_i, R/B.

Appendix C. Comparison between one- and two-sided filtering

We can use our theoretical model to quantitatively compare the situations for one- and two-sided filtering. In particular, we show that the gain in pair rate obtained by removing the loss caused by the filters typically does not justify the strong reduction of the cross-correlation.

Suppose that only the idler photon is filtered. This can be introduced into the formulas of equation (B.19) by substituting Γ_s with $\Gamma_s{}' \gg \Gamma_i$, and η_s with $\eta_s{}' = \eta_s/\eta_{\mathrm{filt}}$, where $\eta_{\mathrm{filt}} = 0.72$ is the peak transmission of the combination of etalon and VBG. After this substition, the modified pair rate can be approximated by

$$W_2{}' \approx \frac{1}{4}\frac{\eta_s}{\eta_{\mathrm{filt}}}\eta_i\frac{R}{B}\Gamma_i = W_2\frac{1}{\eta_{\mathrm{filt}}}\frac{\Gamma_s + \Gamma_i}{\Gamma_s}. \tag{C.1}$$

In our experiment, $\Gamma_s = 2.5\,\Gamma_i$, so switching to one-sided filtering would improve the pair rate by a factor of 2.

Neglecting, for simplicity, detector dark counts, the expression for the zero-delay cross-correlation function reduces to

$$g_{\mathrm{si}}^{(2)}(0) = 1 + 4\tilde{f}_{\mathrm{si}}(0)\frac{B}{R}\frac{\Gamma_s\Gamma_i}{(\Gamma_s + \Gamma_i)^2}, \tag{C.2}$$

which is independent of the filter transmission. Note that the highest cross-correlation is achieved for $\Gamma_s = \Gamma_i$. For $\Gamma_s{}' \gg \Gamma_i$, on the other hand, the modified cross-correlation is approximately

$$\left[g_{\mathrm{si}}^{(2)}\right]'(0) \simeq 1 + 4\tilde{f}_{\mathrm{si}}(0)\frac{B}{R}\frac{\Gamma_i}{\Gamma_s{}'}. \tag{C.3}$$

Without filtering of the signal photon $\Gamma_s{}'$ is on the order of the phase-matching bandwidth, which is three orders of magnitude larger than Γ_i, practically removing any correlations. This is because the pair rate becomes negligible compared to the accidental coincidences caused by the large amount of unfiltered signal photons.

The visibility of the sinusoidal fringes used to characterizate the entanglement in section 7 is related to the cross-correlation function via $V = (g_{\mathrm{si}}^{(2)} - 1)/(g_{\mathrm{si}}^{(2)} + 1)$. Hence, a reduction of the cross-correlation entails a lower-quality entanglement.

Appendix D. Details for the violation of the CHSH inequality

The violation of the CHSH inequality requires the joint measurement of the signal and idler photons in four combinations of bases. In our case, we chose the idler bases X_1 and X_2 to correspond to the Pauli matrices σ_x and σ_y, respectively. If the source would produce the Bell state $|\Phi^+\rangle$, i.e. equation (7) with $\phi = 0$, an optimal choice for the signal photon could be $Y_{1,2} = (\sigma_x \pm \sigma_y)/\sqrt{2}$. For non-zero ϕ, this can be generalized to $Y_{1,2} = \cos\theta_{\pm}\sigma_x + \sin\theta_{\pm}\sigma_y$ with $\theta_{\pm} = \phi \pm \pi/4$. In the experiment, we first determined ϕ by a separate measurement and then proceeded to the violation of the CHSH inequality, which consists of measuring the four correlators

$$E\left(X_{\mathrm{i}},\,Y_{\mathrm{i}}\right)=\frac{N_{11}+N_{22}-N_{12}-N_{21}}{N_{11}+N_{22}+N_{12}+N_{21}},\tag{D.1}$$

where, e.g., N_{11} is the number of coincidences between detectors Si_1 and $\mathrm{ID220}_1$. The CHSH parameter is then given by

$$S=\left|E\left(X_1,\,Y_1\right)+E\left(X_1,\,Y_2\right)+E\left(X_2,\,Y_1\right)-E\left(X_2,\,Y_2\right)\right|.\tag{D.2}$$

We obtained the following values for the correlators

$$E\left(X_1,\,Y_1\right)=0.638(5),$$
$$E\left(X_1,\,Y_2\right)=0.702(5),$$
$$E\left(X_2,\,Y_1\right)=0.700(5),$$
$$E\left(X_2,\,Y_2\right)=-0.669(5)$$

which gives $S=2.708(9)$.

References

[1] Bussières F, Sangouard N, Afzelius M, de Riedmatten H, Simon C and Tittel W 2013 Prospective applications of optical quantum memories *J. Mod. Opt.* **60** 1519–37

[2] Briegel H-J, Dür W, Cirac J I and Zoller P 1998 Quantum repeaters: the role of imperfect local operations in quantum communication *Phys. Rev. Lett.* **81** 5932–5

[3] Sangouard N, Simon C, de Riedmatten H and Gisin N 2011 Quantum repeaters based on atomic ensembles and linear optics *Rev. Mod. Phys.* **83** 33–80

[4] Simon C, de Riedmatten H, Afzelius M, Sangouard N, Zbinden H and Gisin N 2007 Quantum repeaters with photon pair sources and multimode memories *Phys. Rev. Lett.* **98** 190503

[5] Radnaev A G, Dudin Y O, Zhao R, Jen H H, Jenkins S D, Kuzmich A and Kennedy T A B 2010 A quantum memory with telecom-wavelength conversion *Nat. Phys.* **6** 894–9

[6] Ikuta R, Kusaka Y, Kitano T, Kato H, Yamamoto T, Koashi M and Imoto N 2011 Wide-band quantum interface for visible-to-telecommunication wavelength conversion *Nat. Commun.* **2** 537

[7] Zaske S *et al* 2012 Visible-to-telecom quantum frequency conversion of light from a single quantum emitter *Phys. Rev. Lett.* **109** 147404

[8] de Greve K *et al* 2012 Quantum-dot spin-photon entanglement via frequency downconversion to telecom wavelength *Nature* **491** 421–5

[9] Pelc J S *et al* 2012 Downconversion quantum interface for a single quantum dot spin and 1550 nm single-photon channel *Opt. Express* **20** 27510–9

[10] Albrecht B, Farrera P, Fernandez-Gonzalvo X, Cristiani M and de Riedmatten H 2014 A waveguide frequency converter connecting rubidium-based quantum memories to the telecom c-band *Nat. Commun.* **5** 02

[11] Akiba K, Kashiwagi K, Arikawa M and Kozuma M 2009 Storage and retrieval of nonclassical photon pairs and conditional single photons generated by the parametric down-conversion process *New J. Phys.* **11** 013049

[12] Piro N, Rohde F, Schuck C, Almendros M, Huwer J, Ghosh J, Haase A, Hennrich M, Dubin F and Eschner J 2011 Heralded single-photon absorption by a single atom *Nat. Phys.* **7** 17–20

[13] Bao X-H, Qian Y, Yang J, Zhang H, Chen Z-B, Yang T and Pan J-W 2008 Generation of narrow-band polarization-entangled photon pairs for atomic quantum memories *Phys. Rev. Lett.* **101** 190501

[14] Zhang H *et al* 2011 Preparation and storage of frequency-uncorrelated entangled photons from cavity-enhanced spontaneous parametric downconversion *Nat. Photonics* **5** 628–32

[15] Scholz M, Koch L and Benson O 2009 Statistics of narrow-band single photons for quantum memories generated by ultrabright cavity-enhanced parametric down-conversion *Phys. Rev. Lett.* **102** 063603

[16] Fekete J, Rieländer D, Cristiani M and de Riedmatten H 2013 Ultranarrow-band photon-pair source compatible with solid state quantum memories and telecommunication networks *Phys. Rev. Lett.* **110** 220502

[17] Rieländer D, Kutluer K, Ledingham P M, Gündoğan M, Fekete J, Mazzera M and de Riedmatten H 2014 Quantum storage of heralded single photons in a praseodymium-doped crystal *Phys. Rev. Lett.* **112** 040504

[18] Pomarico E, Sanguinetti B, Gisin N, Thew R, Zbinden H, Schreiber G, Thomas A and Sohler W 2009 Waveguide-based OPO source of entangled photon pairs *New J. Phys.* **11** 113042

[19] Pomarico E, Sanguinetti B, Osorio C I, Herrmann H and Thew R T 2012 Engineering integrated pure narrow-band photon sources *New J. Phys.* **14** 033008

[20] Förtsch M, Fürst J U, Wittmann C, Strekalov D, Aiello A, Chekhova M V, Silberhorn C, Leuchs G and Marquardt C 2013 A versatile source of single photons for quantum information processing *Nat. Commun.* **4** 1818

[21] Luo K-H, Herrmann H, Krapick S, Ricken R, Quiring V, Suche H, Sohler W and Silberhorn C 2013 Two-color narrowband photon pair source with high brightness based on clustering in a monolithic waveguide resonator arXiv:1306.1756

[22] Afzelius M, Simon C, de Riedmatten H and Gisin N 2009 Multimode quantum memory based on atomic frequency combs *Phys. Rev.* A **79** 052329

[23] Clausen C, Usmani I, Bussières F, Sangouard N, Afzelius M, de Riedmatten H and Gisin N 2011 Quantum storage of photonic entanglement in a crystal *Nature* **469** 508

[24] Usmani I, Clausen C, Bussières F, Sangouard N, Afzelius M and Gisin N 2012 Heralded quantum entanglement between two crystals *Nat. Photonics* **6** 234–7

[25] Clausen C, Bussières F, Afzelius M and Gisin N 2012 Quantum storage of heralded polarization qubits in birefringent and anisotropically absorbing materials *Phys. Rev. Lett.* **108** 190503

[26] Bussières F *et al* 2014 Quantum teleportation from a telecom-wavelength photon to a solid-state quantum memory *Nat. Photonics* 215

[27] Saglamyurek E, Sinclair N, Jin J, Slater J A, Oblak D, Bussières F, George M, Ricken R, Sohler W and Tittel W 2011 Broadband waveguide quantum memory for entangled photons *Nature* **469** 512–5

[28] Kwiat P G, Mattle K, Weinfurter H, Zeilinger A, Sergienko A V and Shih Y 1995 New high-intensity source of polarization-entangled photon pairs *Phys. Rev. Lett.* **75** 4337–41

[29] Kwiat P G, Waks E, White A G, Appelbaum I and Eberhard P H 1999 Ultrabright source of polarization-entangled photons *Phys. Rev.* A **60** 773–6

[30] Trojek P and Weinfurter H 2008 Collinear source of polarization-entangled photon pairs at nondegenerate wavelengths *Appl. Phys. Lett.* **92** 211103

[31] Kim T, Fiorentino M and Wong F N C 2006 Phase-stable source of polarization-entangled photons using a polarization sagnac interferometer *Phys. Rev.* A **73** 012316

[32] Hentschel M, Hübel H, Poppe A and Zeilinger A 2009 Three-color sagnac source of polarization-entangled photon pairs *Opt. Express* **17** 23153–9

[33] Kwiat P G, Eberhard P H, Steinberg A M and Chiao R Y 1994 Proposal for a loophole-free bell inequality experiment *Phys. Rev.* A **49** 3209–20

[34] Kim Y-Ho, Kulik S P and Shih Y 2001 Bell-state preparation using pulsed nondegenerate two-photon entanglement *Phys. Rev.* A **63** 060301

[35] Palittapongarnpim P, MacRae A and Lvovsky A I 2012 Note: A monolithic filter cavity for experiments in quantum optics *Rev. Sci. Instrum.* **83** 066101

[36] Kato K and Takaoka E 2002 Sellmeier and thermo-optic dispersion formulas for KTP *Appl. Opt.* **41** 5040–4

[37] Jundt D H 1997 Temperature-dependent sellmeier equation for the index of refraction, n_e, in congruent lithium niobate *Opt. Lett.* **22** 1553–5

[38] Ciapurin I V, Drachenberg D R, Smirnov V I, Venus G B and Glebov L B 2012 Modeling of phase volume diffractive gratings, part 2: reflecting sinusoidal uniform gratings, bragg mirrors *Opt. Eng.* **51** 058001

[39] Kuzmich A, Bowen W P, Boozer A D, Boca A, Chou C W, Duan L-M and Kimble H J 2003 Generation of nonclassical photon pairs for scalable quantum communication with atomic ensembles *Nature* **423** 731–4

[40] Razavi M, Söllner I, Bocquillon E, Couteau C, Laflamme R and Weihs G 2009 Characterizing heralded single-photon sources with imperfect measurement devices *J. Phys. B: At. Mol. Opt. Phys.* **42** 114013

[41] Wong F N C, Shapiro J H and Kim T 2006 Efficient generation of polarization-entangled photons in a nonlinear crystal *Laser Phys.* **16** 1517–24

[42] Mitchell M W 2009 Parametric down-conversion from a wave-equation approach: geometry and absolute brightness *Phys. Rev.* A **79** 043835

[43] Christ A, Laiho K, Eckstein A, Cassemiro K N and Silberhorn C 2011 Probing multimode squeezing with correlation functions *New J. Phys.* **13** 033027

[44] Eberly J H 2006 Schmidt analysis of pure-state entanglement *Laser Phys.* **16** 921–6

[45] Peres A 1996 Separability criterion for density matrices *Phys. Rev. Lett.* **77** 1413–5

[46] Clauser J F, Horne M A, Shimony A and Holt R A 1969 Proposed experiment to test local hidden-variable theories *Phys. Rev. Lett.* **23** 880–4

[47] Krapick S, Herrmann H, Quiring V, Brecht B, Suche H and Silberhorn Ch 2013 An efficient integrated two-color source for heralded single photons *New J. Phys.* **15** 033010

[48] Herrmann H, Yang X, Thomas A, Poppe A, Sohler W and Silberhorn C 2013 Post-selection free, integrated optical source of non-degenerate, polarization entangled photon pairs *Opt. Express* **21** 27981–91